




Improved bounds on entropy production in living systems

Dominic J. Skinner^a and Jörn Dunkel^{a,1} 

^aDepartment of Mathematics, Massachusetts Institute of Technology, Cambridge, MA 02139

Edited by Charles S. Peskin, New York University, New York, NY, and approved March 30, 2021 (received for review November 24, 2020)

Living systems maintain or increase local order by working against the second law of thermodynamics. Thermodynamic consistency is restored as they consume free energy, thereby increasing the net entropy of their environment. Recently introduced estimators for the entropy production rate have provided major insights into the efficiency of important cellular processes. In experiments, however, many degrees of freedom typically remain hidden to the observer, and, in these cases, existing methods are not optimal. Here, by reformulating the problem within an optimization framework, we are able to infer improved bounds on the rate of entropy production from partial measurements of biological systems. Our approach yields provably optimal estimates given certain measurable transition statistics. In contrast to prevailing methods, the improved estimator reveals nonzero entropy production rates even when nonequilibrium processes appear time symmetric and therefore may pretend to obey detailed balance. We demonstrate the broad applicability of this framework by providing improved bounds on the energy consumption rates in a diverse range of biological systems including bacterial flagella motors, growing microtubules, and calcium oscillations within human embryonic kidney cells.

entropy production | bacterial motors | microtubules | calcium oscillations | Markov processes

Thermodynamic laws place fundamental limits on the efficiency and fitness of living systems (1, 2). To maintain cellular order and perform essential biological functions such as sensing (3–6), signaling (7), replication (8, 9) or locomotion (10), organisms consume energy and dissipate heat. In doing so, they increase the entropy of their environment (2), in agreement with the second law of thermodynamics (11). Obtaining reliable estimates for the energy consumption and entropy production in living matter holds the key to understanding the physical boundaries (12–14) that constrain the range of theoretically and practically possible biological processes (3). Recent experimental (6, 15, 16) and theoretical (17–20) advances in the imaging and modeling of cellular and subcellular dynamics have provided groundbreaking insights into the thermodynamic efficiency of molecular motors (14, 21), biochemical signaling (16, 22, 23) and reaction (24) networks, and replication (9) and adaption (25) phenomena. Despite such major progress, however, it is also known that the currently available entropy production estimators (26, 27) can fail under experimentally relevant conditions, especially when only a small set of observables is experimentally accessible or nonequilibrium transport currents (28–30) vanish.

To help overcome these limitations, we introduce here a generic optimization framework that can produce significantly improved bounds on the entropy production in living systems. We will prove that these bounds are optimal given certain measurable statistics. From a practical perspective, our method requires observations of only a few coarse-grained state variables of an otherwise hidden Markovian network. We demonstrate the practical usefulness by determining improved entropy production bounds for bacterial flagella motors (10, 31), growing microtubules (32, 33), and calcium oscillations (7, 34) in human embryonic kidney cells.

Generally, entropy production rates can be estimated from the time series of stochastic observables (35). Thermal equilibrium systems obey the principle of detailed balance, which means that every forward trajectory is as likely to be observed as its time reversed counterpart, neutralizing the arrow of time (36). By contrast, living organisms operate far from equilibrium, which means that the balance between forward and reversed trajectories is broken and net fluxes may arise (1, 37–39). When all microscopic details of a nonequilibrium system are known, one can measure the rate of entropy production by comparing the likelihoods of forward and reversed trajectories in sufficiently large data samples (35, 36). However, in most if not all biophysical experiments, many degrees of freedom remain hidden to the observer, demanding methods (28, 40, 41) that do not require complete knowledge of the system. A powerful alternative is provided by thermodynamic uncertainty relations (TURs), which use the mean and variance of steady-state currents to bound entropy production rates (18, 19, 26, 42–48). Although highly useful when currents can be measured (44–47), or when the system can be externally manipulated (40, 49), these methods give, by construction, trivial zero bounds for current-free nonequilibrium systems, such as driven one-dimensional (1D) nonperiodic oscillators. In the absence of currents, potential asymmetries in the forward and reverse trajectories can still be exploited to bound the entropy production rate (29, 30, 50), but to our knowledge no existing method is capable of producing nonzero bounds when forward and reverse trajectories are statistically identical. Moreover, even though previous bounds can become tight in some cases (51), optimal entropy production estimators for nonequilibrium systems are in general unknown.

Significance

Thermodynamic laws fundamentally limit the efficiency and accuracy of living systems. To perform essential functions, from sensing to replication and locomotion, organisms consume energy and dissipate heat. The rate at which they consume energy can be bounded, in theory, by measuring all their internal variables. In practice, however, the entire system is rarely experimentally observable, and many internal states remain hidden. Here, we introduce a mathematical framework that yields optimal bounds on the energy consumption rate when only a small number of observables are available. Overcoming previous limitations, our approach discovers nonzero bounds even when the observed trajectories are time symmetric. We demonstrate the practical usefulness of this method in applications to a variety of recent experimental data.

Author contributions: D.J.S. and J.D. designed research; D.J.S. performed research; and D.J.S. and J.D. wrote the paper.

The authors declare no competing interest.

This article is a PNAS Direct Submission.

Published under the [PNAS license](#).

¹To whom correspondence may be addressed. Email: dunkel@mit.edu.

This article contains supporting information online at <https://www.pnas.org/lookup/suppl/doi:10.1073/pnas.2024300118/-DCSupplemental>.

Published April 27, 2021.

To obtain bounds that are provably optimal under reasonable conditions on the available data, we reformulate the problem here within an optimization framework. Formally, we consider any steady-state Markovian dynamics for which only coarse-grained variables are observable, where these observables may appear non-Markovian. We then search over all possible underlying Markovian systems to identify the one which minimizes the entropy production rate while obeying the observed statistics. More specifically, our algorithmic implementation leverages information about successive transitions, allowing us to discover nonzero bounds on entropy production even when the coarse-grained statistics appear time symmetric. We demonstrate this for both synthetic test data and experimental data (52) for flagella motors. Subsequently, we consider the entropy production of microtubules (33), which slowly grow before rapidly shrinking in steady state, to show how refined coarse graining in space and time leads to improved bounds. The final application to calcium oscillations in human embryonic kidney cells (34) illustrates how external stimulation with drugs can increase entropy production.

Results

Theoretical Background. Due to the large number of particles involved, classical thermodynamics can reasonably treat macroscopic processes, like a combustion cycle in an engine, as deterministic. By contrast, theoretical descriptions of microbiological processes such as intracellular stochastic reactions (24, 53), cellular sensing (4, 25, 54), and DNA transcription and repair (55, 56) must account for fluctuations (1, 57). The most widely used framework (17, 58, 59) for this purpose is probabilistic Markov models that assume stochastic transitions between states (60) (Fig. 1). Specifically, for the mesoscopic biophysical systems studied below, there is a time-scale separation between the fast degrees of freedom of the environment, such as the positions and momenta of the solvent molecules, and the slow degrees of freedom of the system of interest, such as the length of a microtubule or the concentration of calcium ions. This scale separation allows for an effective description as Markovian dynamics over the slow degrees of freedom (28). We further note that, in this case, the non-Markovian nature of experimentally accessible observables does not arise through measurements on time scales close to the bath correlation time scale (61), but rather from partial “coarse-grained” observations (Fig. 1); an underlying Markovian description of the complete set of slow degrees of freedom remains appropriate. Within this framework, stochastic thermodynamics was introduced (24, 35, 57) and is now well validated experimentally (62–65). Recent efforts have thus turned to the problem of thermodynamic inference: deducing thermodynamic quantities, such as the entropy production rate, from partial observations (19, 27). The improved estimators introduced here perform this inference by bounding from below the entropy production rate of any coarse-grained Markovian system, whether it be discrete or continuous in space (66) (*SI Appendix, section IX*) or observed only at discrete times (*SI Appendix, section VII*).

Exact Entropy Production Rate. Our goal is to construct an estimator that comes as close as possible to the true entropy production rate σ of the underlying Markov network, which remains hidden to us. The only assumptions we shall make are that the microscopic state network is connected, that transitions between states are reversible as required by thermodynamics (19), and that there is no external time-dependent driving, so that the microscopic system S will reach a unique steady state in which it spends a fraction π_i of the time in state i . A system in thermal equilibrium obeys detailed balance, meaning forward and reverse transitions are equally likely to be observed, or $\pi_i q_{ij} = \pi_j q_{ji}$, where q_{ij} is the rate at which the system transitions from

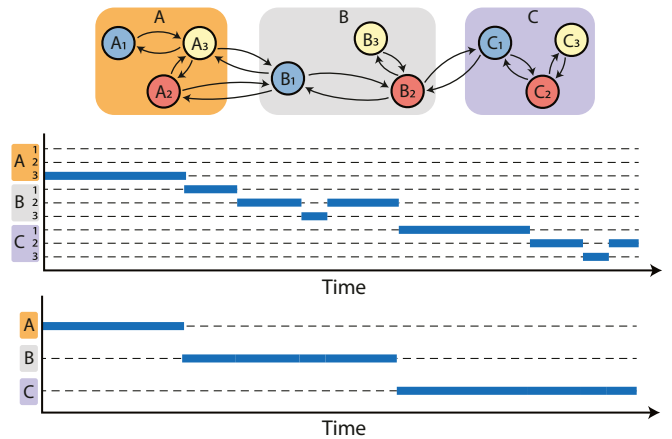


Fig. 1. Illustration of an underlying Markovian transition network and the coarse-grained observed system. The microscopic Markovian system (*Top*) contains nine states labeled A_1, \dots, C_3 , while the observer can only distinguish the coarse-grained macrostates A, B, C and transitions between them. Shown are a sample trajectory on microstates of the system (*Middle*) and the observed macrostate trajectory (*Bottom*), which in general exhibits non-Markovian transition dynamics.

microstate i to microstate j (19). For systems in a nonequilibrium steady state (NESS), violations of detailed balance occur at the price of increasing entropy of their environment. The associated rate of entropy production $\sigma(S)$ is formally given by

$$\sigma = k_B \sum_{i \neq j} \pi_i q_{ij} \log \left(\frac{q_{ij}}{q_{ji}} \right), \quad [1]$$

where $\pi_i q_{ij}$ counts the rate of transitions $i \rightarrow j$, and $k_B \log(q_{ij}/q_{ji})$ counts the entropy change for such a transition (19). In principle, given all of the states and a sufficiently long system trajectory, we could deduce the values of π_i and q_{ij} and hence calculate σ exactly from Eq. 1. In practice, however, one typically cannot know or observe all of the states, and experimental time-series measurements are possible only for severely coarse-grained macroscopic observables (Fig. 1). The challenge is then to estimate σ from such coarse-grained data.

Coarse-Grained Observables Can Be Non-Markovian. We observe the coarse-grained macrotrajectories of an underlying Markovian microscopic process, which formally can be treated as the output of a hidden Markov model (67, 68). In contrast to the underlying Markovian system, the output need not be Markovian, semi-Markovian, second-order Markovian, or even N th-order Markovian for any N (29, 69, 70) (*SI Appendix, section II*). The set of macroscopic observables, $\mathcal{O}(S)$, therefore contains infinitely many measurements. For instance, for the example process in Fig. 1, one could measure $\hat{\pi}_A$, the fraction of the time spent in macrostate A , or $\hat{\pi}_A \hat{q}_{AB}$, the rate at which $A \rightarrow B$ transitions are observed, meaning that if the system was observed for a long time T , one would expect to see $T \hat{\pi}_A \hat{q}_{AB}$, $A \rightarrow B$ transitions (*SI Appendix, section II*). One could also measure more complex quantities, like $\hat{\pi}_A \hat{q}_{ABC \dots A}$, the rate at which trajectories are observed to take the arbitrarily long path $ABC \dots A$; such observables do not necessarily follow from simpler statistics.

Bounding Entropy Production by Solving a Minimization Problem. To reformulate the estimation of $\sigma(S)$ as a tractable optimization problem, let us first suppose that we are given all quantities in $\mathcal{O}(S)$. In this case, we know that the true entropy production

rate of the system \mathcal{S} is at least as large as the minimum entropy production of all systems \mathcal{R} with the same observed statistics

$$\sigma(\mathcal{S}) \geq \min \{ \sigma(\mathcal{R}) | \mathcal{O}(\mathcal{R}) = \mathcal{O}(\mathcal{S}) \}. \quad [2]$$

In particular, this bound is the best possible bound without knowing further details of the underlying network topology and hence the best possible estimator.

In practice, it is only feasible to measure a select few quantities in \mathcal{O} , but from these we can build a similar estimator. Specifically, given a set \mathcal{O}_k , containing a subset of the total observables \mathcal{O} , we still have that

$$\sigma(\mathcal{S}) \geq \min \{ \sigma(\mathcal{R}) | \mathcal{O}_k(\mathcal{R}) = \mathcal{O}_k(\mathcal{S}) \}, \quad [3]$$

where the new estimator on the right-hand side is the optimal bound given this smaller set of observables. Note that fewer observables provide fewer restrictions on the set of possible microsystems \mathcal{R} , meaning that the bound in Eq. 3 is lower than that in Eq. 2.

One-Step Estimator. A simple useful observable subset is $\mathcal{O}_1 = \{ \hat{\pi}_I \hat{q}_{IJ} \}$, containing the rates at which transitions $I \rightarrow J$ happen for all pairs of observed macrostates (I, J) . For the specific network topology in Fig. 1, the observed statistic $\hat{\pi}_A \hat{q}_{AB} \in \mathcal{O}_1$ simply counts the rate at which $A \rightarrow B$ transitions are observed and can be expressed in terms of the microstates as $\hat{\pi}_A \hat{q}_{AB} = \pi_{A_2} q_{A_2 B_1} + \pi_{A_3} q_{A_3 B_1}$. Despite having to minimize over infinitely many network topologies \mathcal{R} consistent with the \mathcal{O}_1 statistics, finding the corresponding estimator σ_1 is straightforward. This is due to the fact that, given any network topology consistent with \mathcal{O}_1 , one can modify this topology by combining two microstates in the same macrostate, in such a way that one preserves the \mathcal{O}_1 statistics, while lowering the entropy production rate (SI Appendix, section III). By repeatedly applying this procedure, the resulting system has no hidden states, every macrostate corresponds to exactly one microstate, and the entropy production rate of this system can therefore be calculated directly. The estimator σ_1 coincides with known estimators, \dot{S}_{aff} in ref. 29 and relative entropy of 2-strings in ref. 30, but was not previously treated within an optimization framework. However, it turns out that substantially improved entropy production bounds can be obtained by combining information from two successive transition steps (Fig. 2).

Two-Step Estimator. To go beyond \mathcal{O}_1 statistics, we consider the set $\mathcal{O}_2 = \mathcal{O}_1 \cup \{ \hat{\pi}_I \hat{q}_{IJK} \}$, containing the rates at which two successive transitions $I \rightarrow J \rightarrow K$ occur for all triplets (I, J, K) , so that after a long time T , one would expect to see $T \hat{\pi}_I \hat{q}_{IJK}$ transitions $I \rightarrow J \rightarrow K$. Knowledge of \mathcal{O}_2 imposes stronger constraints on the set of underlying Markov processes \mathcal{R} , promising a better bound on the entropy production rate. In practice, performing a direct numerical minimization to obtain the corresponding estimator σ_2 is not possible due to the arbitrary complexity of permissible Markovian network topologies \mathcal{R} ; each macrostate of \mathcal{R} could contain arbitrarily many microstates and so contain arbitrarily many transition rates to be optimized over. However, two exact analytic results, proved in SI Appendix, section IV, enable us to find the best possible bound for the combined entropy production across all edges connected to a state J , while preserving the \mathcal{O}_2 statistics $\pi_I q_{IJ}, \pi_J q_{JI}, \pi_I q_{JK}$ for any distinct neighboring macrostates I, K . Specifically, our first result enables us to take any network \mathcal{R} consistent with \mathcal{O}_2 and simplify its internal topology so that only J has hidden states and, further, that J has no internal connections. We show (SI Appendix, section IV) that one can always construct the simplified network in such a way that the entropy production rate is lowered while remaining consistent with the \mathcal{O}_2 statistics involving J . Our second result proves that minimizing over this simplified topology, with arbitrarily many internal states of J , yields the same bound as minimizing over a system with six internal states for each pair of neighboring macrostates (I, K) . This fact makes the problem numerically tractable (71, 72) (SI Appendix, section IV). By bounding the entropy production rate across connecting edges for every macrostate in this manner, we get a σ_2 bound for the total entropy production. This new estimator satisfies the hierarchy $\sigma \geq \sigma_2 \geq \sigma_1$ and only makes use of statistics which can be computed by observing the states visited by a suitably long trajectory without utilizing harder to measure statistics, such as nonexponential waiting time distributions (29) (SI Appendix, section VI).

Bounding Entropy Production for Time Symmetric Observables. We demonstrate the performance of σ_2 relative to other estimators for a physically and biologically relevant test process, corresponding to a biased random walk that switches with rate r between two modes of bias (Fig. 2). This process represents a minimal model for the discretized angular dynamics of

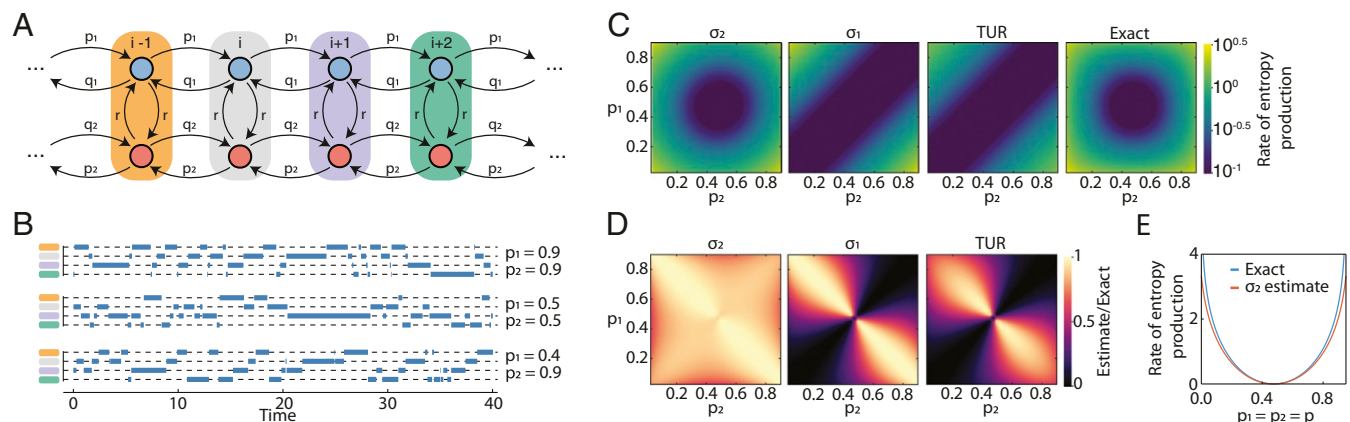


Fig. 2. The two-step estimator σ_2 outperforms other estimators for the switching biased random walk. (A) Diagram for the underlying Markovian dynamics, with blue and red circles representing internal states and shaded regions representing the observed macrostates, $i, \dots, i+3$. All waiting time distributions are exponential with mean $\lambda = 1$, implying that $1 = r + p_1 + q_1 = r + p_2 + q_2$. Throughout this diagram, we fix $r = 0.05$, so that specifying p_1 and p_2 is sufficient to describe the system. (B) Sample trajectories for different values of p_1 and p_2 in a periodic network with four observed states. (C) σ_2 , σ_1 , and TUR estimates versus the exact entropy production rates in the (p_1, p_2) plane. (D) The ratios between estimates and true values show that the σ_2 estimator provides a close fit for all values of p_1 and p_2 , whereas the other estimators perform well only for certain combinations of transition rates. (E) In the time-symmetric case $p_1 = p_2 = p$, the σ_2 estimates closely bound the exact values, whereas the other estimators give trivial zero bounds.

a bacterial motor that switches rotation direction (31, 73). It can also describe a particle subjected to a flashing force (74) or, more generally, active Brownian on a lattice (75). As shown in Fig. 2A, when fixing the internal transition rate r and assuming exponential waiting time distributions with equal means on all internal states, the model dynamics are controlled by the two transition rate parameters p_1 and p_2 , describing right and left jumps, respectively. Coarse-grained sample trajectories, corresponding to observations of four macrostates for different combinations of p_1 and p_2 , are shown in Fig. 2B. In the special case $p_1 = 1 - r - p_2$, we recover a biased random walk, or Brownian clock if made periodic (13), which has effectively no hidden states. Alternatively, if $p_1 = p_2 = p$, the observed system—despite being out of equilibrium for all but one value of p —is completely time symmetric with every forward path as likely to appear as every reverse path, implying vanishing net fluxes.

To illustrate the benefits of leveraging multistep information, we compare σ_2 to the one-step estimator σ_1 and also with entropy production rate estimates from the TUR (18, 19, 26), where the TUR is a general relation between the fluctuations of, potentially coarse-grained, currents and the entropy production rate, which can be used as an estimator (SI Appendix, section VII). We find that in the strong-flux regime, when p_1 and p_2 are sufficiently different, all estimators reasonably bound the true entropy production rate σ from Eq. 1 (Fig. 2C and D). However, as p_1 and p_2 approach each other and the net flux becomes weaker, only σ_2 gives an accurate bound (Fig. 2D). In particular, when $p_1 = p_2 = p$, the forward and reverse observables are time symmetric, so the relative entropy between them is zero (29). Therefore, neither σ_1 , which here coincides with the estimator \dot{S}_{KLD} in ref. 29, nor the TUR can yield a nontrivial (nonzero) bound, whereas σ_2 can be computed analytically in this case (SI Appendix, section VII) and approximates the exact rate σ well for all values of p (Fig. 2E). We next apply the two-step estimator σ_2 to data from recent experiments.

Switching Trajectories of Bacterial Flagellar Motor. By rotating helical flagella, many species of bacteria can swim, reaching speeds of tens of body lengths per second (10, 76). Each flagellum is driven by a remarkable nanoscale motor, powered by a flux of ions across the cytoplasmic membrane, which can achieve over 100 rotations per second (31, 76, 77). Measuring the entropy production of the motor promises insights into the efficiency of small self-assembled engines and microbial locomotion (10, 58, 78). Direct experimental observations of the motor dynam-

ics have become possible by tethering the cell, attaching a bead to the flagellum, and tracking the bead trajectory through high-resolution microscopy (31, 52, 79, 80). The motor-and-bead system operates in a heat bath at finite temperature, and the observed bead trajectories can be described by Markovian Langevin-type dynamics (10). The bead trajectories are observed only at a finite frame rate, so the exact coarse-grained transition rates cannot be measured. However, applying the estimators σ_1 and σ_2 directly to the resulting coarse-grained in time system still results in a lower bound for the entropy production rate (SI Appendix, section VIII).

A representative bead trajectory for an *Escherichia coli* bacterium, from a recent experiment by Nirody et al. (52), is shown in Fig. 3A. Measured trajectories typically follow approximately circular curves in the projection plane, but certain strains will stochastically switch their rotation direction (31). This means that, although taking place far from equilibrium, the process may not obviously violate time irreversibility, limiting the applicability of previous entropy production estimators. Bead trajectories provide a coarse-grained view of the motor system—our framework allows us to coarse grain further, dividing the total system radially into three macrostates (Fig. 3B). An accordingly discretized trajectory is shown in Fig. 3C. From a practical perspective, having a smaller number of states can be preferable for acquiring precise transition statistics, especially if data are limited.

We estimated entropy production bounds for two sodium-powered strains of *E. coli*, comparing the nonswitching strain MTB24 at fuel concentrations of 10 mM Na⁺ and 85 mM Na⁺ with the switching strain MTB32 at 85 mM Na⁺ (Materials and Methods). For the nonswitching MTB24 strain, which strongly breaks time-reversal symmetry, the σ_2 bound does not improve significantly on the σ_1 estimate (Fig. 3D). As expected, both estimators find that a higher ion concentration increases the bound on the entropy production rate for the nonswitching MTB24 strain, as higher-frequency rotations were observed. However, for the switching MTB32 strain, we find that the σ_1 significantly underestimates the entropy production rate relative to σ_2 . More specifically, the mean entropy production rate of MTB24 at low fuel concentration 10 mM Na⁺ and MTB32 at high fuel concentration 85 mM Na⁺ cannot be statistically distinguished under the σ_1 estimator ($P < 0.05$; Fig. 3D). By contrast, the σ_2 estimator clearly distinguishes ($P < 0.01$) between the two experiments, yielding high fuel entropy production estimates that are consistent for both strains (Fig. 3D). Corroborating the results from a biased random walk test case, this application highlights the

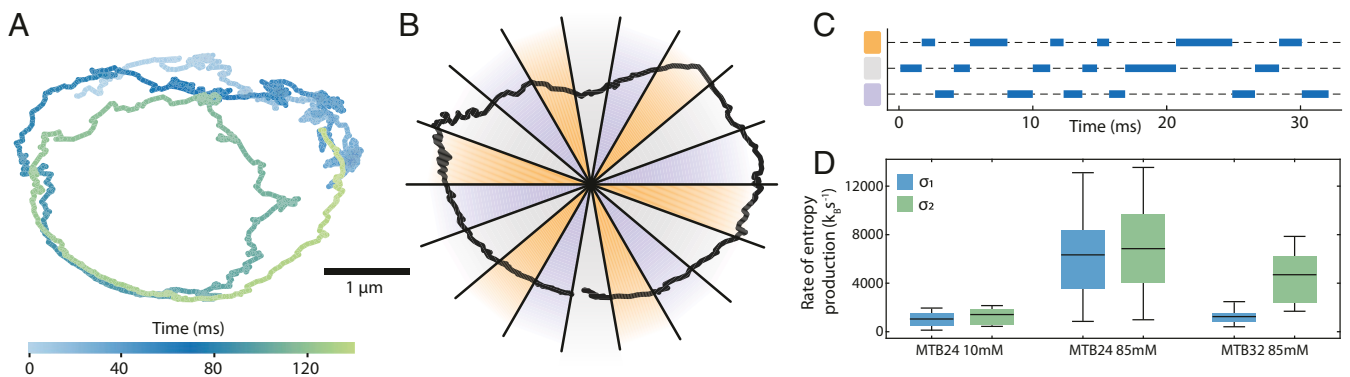


Fig. 3. The estimator σ_2 bounds the rate of entropy production for the bacterial flagellar motor. (A) Short trajectory of bead attached to MTB32 *E. coli* bacteria flagella. The bead begins rotating clockwise, but changes direction after around 30 ms, subsequently rotating counterclockwise. (B) The plane is discretized into three regions (purple, orange, gray), and each region is made of N segments, here $N = 6$. A short bead trajectory is overlaid. (C) The trajectory from B after coarse graining onto the three macrostates. (D) Box plot of entropy production rates for different strains, sodium concentrations, and estimators. The σ_1 estimator measures a similar entropy production rate for MTB24 10 mM and MTB32 85 mM, whereas the σ_2 estimator can distinguish them.

importance of incorporating multitransition information when estimating entropy production for a nonequilibrium system with small net fluxes.

From a broader conceptual perspective, it is worth emphasizing that the entropy production bounds were obtained without assuming any particular model for the motor's dynamics, precise measurements of ion concentrations, or a rheological characterization of the medium. The rate estimates can be used to gain insights into the working principles and fuel consumption of bacterial motors, with σT interpreted as the minimal rate of free energy required to maintain the out-of-equilibrium state (detailed discussion below). For example, measurements of the ion motive force suggest that the free energy change of a single ion transit is around $6k_B T$ (76). Combining this with the estimates in Fig. 3D, we can bound the average rate of ion consumption as $\geq 1,000 \text{ s}^{-1}$ for the 85-mM fuel concentrations.

Dynamic Instability of Microtubule Growth. Microtubules are a core component of eukaryotic cells, providing structural stability, enabling intracellular transport, and facilitating cell division (81, 82). To fulfill these key functions, microtubules must have the ability to rapidly remodel, for both assembly and disassembly (81). They achieve this through dynamic instability: periods of steady growth before switching stochastically into rapid shrinking (32, 83). The rates of growth, shrinkage, and switching are actively regulated to achieve different behaviors (33, 81, 82). While it is known that microtubule growth requires guanosine triphosphate (GTP) hydrolysis (83) and is therefore out of equilibrium, several competing theoretical models of microtubule dynamics predict different entropy production rates (84).

By applying our estimators directly to experimental *in vitro* microtubule images, we can bound the entropy production rate without assuming any particular model for microtubule dynamics. From a stabilized nucleation site, at constant concentration of tubulin and GTP, microtubules will form, grow, shrink, and disappear before reforming some time later (*Materials and Methods*). Kymographs from recent experimental observations (33) show the steady-state trajectories of the microtubule length (Fig. 4A). Since the length oscillates around its mean value along one spatial dimension, the net flux vanishes, so that we have to use σ_2 to obtain a nontrivial entropy production bound. Similar to before, we divide space into three periodically layered regions (Fig. 4B), which yield coarse-grained discretized trajectories as shown in Fig. 4C. Applying σ_2 , we find that a growing microtubule produces entropy at a rate of at least $5k_B \cdot \text{min}^{-1}$. Furthermore, choosing a larger spatial or temporal coarse-graining scale decreases the estimates for the entropy production rate,

as demonstrated in Fig. 4D and E. Conversely, this means that higher-resolution experiments promise improved bounds.

Induced Calcium Oscillations in Human Embryonic Kidney Cells. A coherent cell response to external stimuli requires intracellular signaling (34). One way in which cells encode and transport signal is by controlling the concentration of calcium ions within the cytosol (7, 85). Such calcium oscillations propagate instructions for muscle contraction (86), gene expression (87), and cell differentiation (88). These oscillations appear as calcium concentration spikes, with Ca^{+2} ions being released into the cell before ion pumps remove them again (7, 85). Since ion pumps move Ca^{+2} from a region where the concentration is low (cytosol) to where the concentration is high (sarcoplasmic reticulum) (85), the system operates out of equilibrium. By measuring the ratio of fluorescence at different wavelengths, it is possible to infer the concentration of Ca^{2+} noninvasively within a single living cell (85).

In human embryonic kidney cells, calcium oscillations can be triggered by exposure to carbachol, with the specific response dependent on the concentration of carbachol (85). Recent experiments by Thurley et al. (34) took human embryonic cells and exposed them to a 30- μM concentration of carbachol, which after an initial transient resulted in a statistically steady state of oscillations (Fig. 5A). After 1 h, the cells were restimulated with a higher concentration of carbachol, resulting in a new steady state (Fig. 5A). As before, we coarse grain by discretizing the calcium trajectory into three regions, one containing the default level, one containing intermediate values, and one containing the peaks of the oscillations (Fig. 5A). The coarse-grained trajectories are shown in Fig. 5B. Applying our σ_2 estimator, we find that prior to stimulation the rate of entropy production is at least $4k_B \cdot \text{min}^{-1}$. After exposing the cells to 200 μM carbachol, this bound increases to around $8k_B \cdot \text{min}^{-1}$ (Fig. 5C). As in the microtubule case, a finer coarse graining can be expected to give improved estimates but will also require a finer temporal resolution than currently available.

Discussion

Entropy Production without Relative Entropies. It is often implicitly assumed that the best possible bound on entropy production rate comes from estimating the relative entropies between forward and reverse trajectories, either directly or through TUR (29, 47). To see that nontrivial bounds can be placed on the entropy production rate, even when observable macrostate trajectories appear time symmetric and so relative entropies are zero, consider a simple Markov chain model of a Brownian clock on four

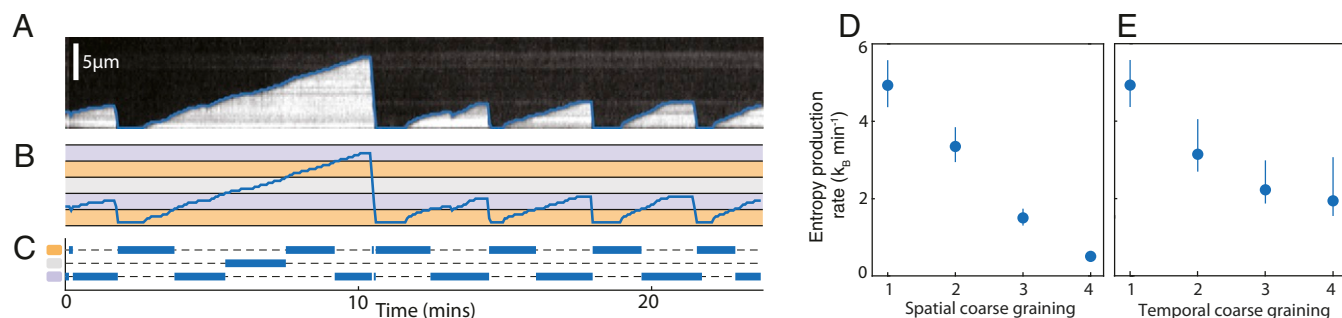


Fig. 4. Bounding the entropy production rate of steady-state microtubule growth. (A) Typical kymograph of growing microtubule showing steady growth, rapid shrinkage until vanishing, and then regrowth after nucleation. Overlaid is the segmented length (blue line). (B) The length trajectory is discretized into three regions which are layered periodically. (C) The corresponding discretized trajectory for the system in B. (D) The largest rate of entropy production is calculated when the regions are 1 pixel tall, and the inferred entropy production decreases for regions of size 2,3,4 pixels. Information is lost due to the finite spatial resolution. Error bars are bootstrapped 95% confidence intervals. (E) Performing a coarse graining in time, taking every second, third, or fourth image, also lowers the inferred entropy production rate, but not as strongly as the spatial coarse graining.

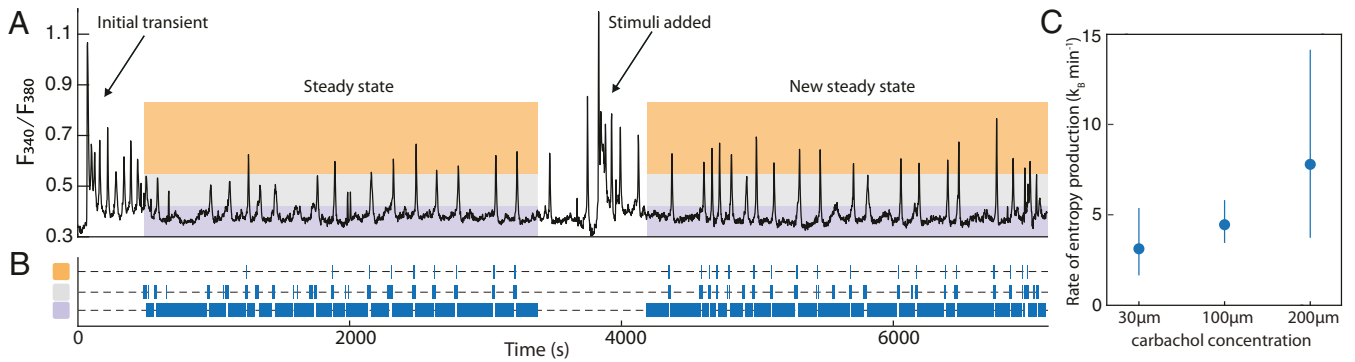


Fig. 5. Bounding the entropy production rate of calcium oscillations within human kidney cells. (A) Ratio of fluorescence at different wavelengths, as a proxy for calcium concentration, against time. Initially cells are exposed to 30- μM carbachol and reach a statistically steady state. After around 1 h they are exposed to a higher level of carbachol and reach a new steady state. During these steady states, we partition space into three regions as shown. (B) Discretized trajectory on the three regions. (C) Bounds computed after the initial 30- μM stimulation and after the subsequent restimulation with 100 or 200 μM carbachol reveal a substantial increase in entropy production in response to the second stimulus. Error bars are bootstrapped 95% confidence intervals.

microstates $\{1, 2, 3, 4\}$, with clockwise transition probabilities q_+ and counterclockwise probabilities $q_- = 1 - q_+$ (13). When $q_+ > q_-$, the full system is not time symmetric; for suitably long observations, a net clockwise current is observed. However, if states 2 and 4 were part of some macrostate H , we are just as likely to observe any forward trajectory on the macrostate set $\{1, 3, H\}$ as its time reverse counterpart. To see this, consider an arbitrary observed trajectory, say $X = (1, H, 3, H, 3, H)$ of length 6. The probability of observing this macrostate trajectory is $\mathbb{P}(X) = \sum_Y \mathbb{P}(Y)$, where the sum is taken over all microstate trajectories Y consistent with the observed macrostate trajectory, which includes $Y = (1, 2, 3, 4, 3, 4)$. Define \bar{Y} to be the trajectory where we take Y and switch states 2 and 4, so $\bar{Y} = (1, 4, 3, 2, 3, 2)$ which has the same macrostate observables. If the microscopic trajectory Y has k clockwise transitions and n counterclockwise transitions, then $\mathbb{P}(Y) = (1/4)q_+^k q_-^{n-k}$, whereas $\mathbb{P}(\bar{Y}) = (1/4)q_+^{n-k} q_-^k$. The time reversed microstate trajectory Y_r has $n - k$ clockwise transitions and k counterclockwise and in general has a different probability of occurring as the forward trajectory. However, $\mathbb{P}(Y_r) + \mathbb{P}(\bar{Y}_r) = \mathbb{P}(Y) + \mathbb{P}(\bar{Y})$, and so the forward and backward macrostate trajectories are equally probable, $\mathbb{P}(X) = \mathbb{P}(X_r)$. Intuitively, from the observed statistics, we know that no reversible Markov chain can behave that way; when entering H from 1, trajectories enter a set of states that typically transition to 3, and vice versa. Therefore, there must be some internal cycles occurring—even though the relative entropy of the macroscopic forward and backward trajectories is zero. For the continuous-time version of this example, we can derive analytically the σ_2 -estimator bound, which coincides in this case with the exact entropy production rate (SI Appendix, section V).

Thermodynamic Interpretation. As our theoretical analysis assumed a NESS, the thermodynamic interpretation of the bounds on σ requires us to revisit precisely whether or not this assumption is valid under relevant experimental conditions. While entropy can be defined more generally along a single stochastic trajectory (17, 89), the average rate of entropy production in a NESS represents the rate of entropy increase in the chemical or thermal reservoirs coupled to the system, which drive the NESS. For isothermal systems, $\sigma = Q_{hk}/T$, where Q_{hk} is the housekeeping heat (35, 90), which quantifies the rate at which heat is dissipated into the environment. Importantly, however, σ can also be interpreted as the minimum rate at which free energy must be consumed to maintain the NESS (59, 90). Some of the experiments analyzed here represent a quasistationary state (QSS) rather than a true NESS. For

instance, the concentration of Na^+ is not replenished in the bacterial motor experiments but also does not appreciably change over the observation period. While the distinction is subtle, the interpretation of σT as the physical heat dissipated while maintaining the system does not hold in a QSS (90). However, even for a QSS, σT still represents the rate at which free energy is consumed (90), and moreover it is this quantity which is of interest, because it represents the effective price to hold the system away from equilibrium. Additionally, if the system converts, say chemical free energy at rate f_{in} , into mechanical energy output at rate f_{out} , then $f_{in} - f_{out} = \sigma T$, and so if either input or output power is known, a bound on entropy production σ directly bounds the efficiency of this process (35, 90).

Entropic Tradeoffs. Entropic costs limit the accuracy of biological sensory systems (5, 91), biological clocks (92), and intrinsic noise suppression in cells (41, 93). Beyond direct applications to experimental data, the current framework can help us understand and quantify tradeoffs between the faithful execution of a biological function and the energy expended to do so (1, 13, 92). In particular, since our approach can establish nontrivial bounds for a single variable with no observable net currents, it may be used to bound the entropic cost of executing a specific function, such as performing oscillations at some frequency and regularity. Furthermore, recent work (41, 94) revealed fundamental limits for suppressing molecular fluctuations within cells through negative feedback loops, finding a tradeoff between control and molecule numbers without making specific assumptions on the nature of the feedback loops. Similarly, the model-agnostic estimators introduced here could be used to infer additional thermodynamic costs of regulating molecular fluctuations by quantifying the entropic tradeoffs cells are forced to make.

Outlook. A practical benefit of the above framework lies in the fact that the coarse-graining level can be adapted to the quality and volume of the available experimental data. In the applications above, we focused coarse graining to a small network with only three remaining states, which makes it easier to collect precise statistics for the transition rates. In general, with increasing data resolution and trajectory length, finer coarse graining of space and time will lead to better bounds. Extrapolating the impressive progress of imaging techniques over the last decade, one can expect that σ_2 -based estimation applied to higher-resolution data will enable rapidly improving entropy production rate estimates in the near future.

Conclusions

Living systems resist their decay into thermal equilibrium by expending entropy to maintain essential cellular processes and functions (41, 53). A quantitative understanding of the associated thermodynamic costs hinges on our ability to infer entropy production rates from partial experimental observations (29). By recasting this inference problem within an optimization framework, we have constructed an improved rate estimator that can be directly applied to coarse-grained observations of steady-state nonequilibrium systems. Our analysis of recent experimental data shows that this approach places more accurate bounds on the entropy production rates without making specific modeling assumptions. By leveraging information contained in successive transitions, the derived two-step estimator overcomes a key limitation of previous estimation schemes that require statistically distinguishable forward and reversed trajectories. As a result, we were able to obtain improved bounds on the entropy production of bacterial motors (52), microtubules (33), and calcium oscillations (34). These successful applications provide guidance for how model-agnostic inference can be used to extract fundamental information from single-variable observations of otherwise hidden intracellular and intercellular processes.

Materials and Methods

Bacteria Flagella Motor. Bacterial flagella bead trajectories were provided by Jasmine Nirody and obtained similarly to the procedure in Nirody et al. (52). In their recent experiments, *E. coli* bacteria were immobilized on a coverslip, and a bead (1 μm) was attached to their shortened flagella. The bead position is found using back focal-plane interferometry (31, 52, 80). The strains MTB24 and MTB32 were used, with the motor powered by sodium ions in both cases. Concentrations were 10-mM and 85 mM Na^+ for MTB24 and 85 mM Na^+ for MTB32. A single trajectory of length 20 s was taken from each experiment, where each 20-s window contained at least 400 rotations, and was sufficiently long to estimate the transition rates. For each trajectory, the origin was taken as the trajectory center of mass in the xy plane. The plane was then divided into three regions made from 3N segments, with N chosen for each trajectory to maximize the entropy

production rate bound. In total, we analyzed 7 MTB24 10-mM trajectories, 25 MTB24 85-mM trajectories, and 10 MTB32 85-mM trajectories.

Microtubule Dynamic Instability. Experimentally measured microtubule trajectories were provided by Benjamin Lacroix, Institut Jacques Monod, CNRS & Université Paris Diderot, France. Stabilized guanylyl 5'- α , β -methylene diphosphonate (GMPCPP) seeds were attached to a functionalized surface and served as nucleation sites. They were placed in a solution of 7 μM tubulin and 1-mM GTP at a temperature of 35 $^\circ\text{C}$. The growing microtubules were imaged by total internal reflection fluorescence (TIRF) microscopy, and kymographs were automatically extracted, from which the microtubule length was calculated. Data from two experiments performed under identical conditions were used in our analysis, with 1,200 min of total observation time, and both experiments were combined to estimate the transition rates.

Calcium Oscillations. The calcium concentration trajectories were taken from recent experiments by Thurley et al. (34), with 20 trajectories for the protocol of 30- μM carbachol stimulation followed by 100- μM carbachol restimulation and 14 trajectories for 30- μM carbachol stimulation followed by 200- μM carbachol restimulation. Trajectories under the same experimental conditions were combined to estimate transition rates. The same concentration coarse graining into three regions was applied to data taken at 30- μM and 100- μM carbachol. The coarse-grained states were adapted for data corresponding to the 200- μM carbachol restimulation, as these tended to be larger in amplitude and displayed higher fluorescence ratio between spikes.

Data Availability. All study data and relevant codes can be downloaded from Github (<https://github.com/Dom-Skinner/ImprovedBoundsOnEntropyProduction>).

ACKNOWLEDGMENTS. We thank Jasmine Nirody for providing the bacterial flagella trajectories, Benjamin Lacroix for sharing the microtubule trajectories, Alexander Skupin for providing the calcium oscillation data, and all of them for explaining their experiments to us. We are also grateful to Massimiliano Esposito and Jordan Horowitz for helpful discussions and insightful comments on an early manuscript draft and to the Banff International Research Station workshop "Mathematical Models in Biology: from Information Theory to Thermodynamics." This work was supported by a MathWorks Fellowship (to D.J.S.), a James S. McDonnell Foundation Complex Systems Scholar Award (to J.D.), and the Robert E. Collins Distinguished Scholar Fund (to J.D.).

1. F. S. Gnesotto, F. Mura, J. Gladrow, C. P. Broedersz, Broken detailed balance and non-equilibrium dynamics in living systems: A review. *Rep. Prog. Phys.* **81**, 066601 (2018).
2. E. Schrödinger, R. Penrose, *What Is Life?: With Mind and Matter and Autobiographical Sketches, Canto Classics* (Cambridge University Press, 2012).
3. B. Hu, W. Chen, W. J. Rappel, H. Levine, Physical limits on cellular sensing of spatial gradients. *Phys. Rev. Lett.* **105**, 048104 (2010).
4. P. Mehta, D. J. Schwab, Energetic costs of cellular computation. *Proc. Natl. Acad. Sci. U.S.A.* **109**, 17978–17982 (2012).
5. G. Lan, Y. Tu, Information processing in bacteria: Memory, computation, and statistical physics: A key issues review. *Rep. Prog. Phys.* **79**, 052601 (2016).
6. B. Nadrowski, P. Martin, F. Jülicher, Active hair-bundle motility harnesses noise to operate near an optimum of mechanosensitivity. *Proc. Natl. Acad. Sci. U.S.A.* **101**, 12195–12200 (2004).
7. D. E. Clapham, Calcium signaling. *Cell* **131**, 1047–1058 (2007).
8. A. Maitra, K. A. Dill, Bacterial growth laws reflect the evolutionary importance of energy efficiency. *Proc. Natl. Acad. Sci. U.S.A.* **112**, 406–411 (2015).
9. J. L. England, Statistical physics of self-replication. *J. Chem. Phys.* **139**, 121923 (2013).
10. J. A. Nirody, Y. R. Sun, C. J. Lo, The biophysicist's guide to the bacterial flagellar motor. *Adv. Phys. X* **2**, 324–343 (2017).
11. S. J. Bryant, B. B. Machta, Energy dissipation bounds for autonomous thermodynamic cycles. *Proc. Natl. Acad. Sci. U.S.A.* **117**, 3478–3483 (2020).
12. G. E. Crooks, Entropy production fluctuation theorem and the nonequilibrium work relation for free energy differences. *Phys. Rev. E* **60**, 2721–2726 (1999).
13. A. C. Barato, U. Seifert, Cost and precision of Brownian clocks. *Phys. Rev. X* **6**, 041053 (2016).
14. P. Pietzonka, A. C. Barato, U. Seifert, Universal bound on the efficiency of molecular motors. *J. Stat. Mech.* **2016**, 124004 (2016).
15. É. Fodor et al., Nonequilibrium dissipation in living oocytes. *Europhys. Lett.* **116**, 30008 (2016).
16. J. Rodenfels, K. M. Neugebauer, J. Howard, Heat oscillations driven by the embryonic cell cycle reveal the energetic costs of signaling. *Dev. Cell* **48**, 646–658.e6 (2019).
17. U. Seifert, Entropy production along a stochastic trajectory and an integral fluctuation theorem. *Phys. Rev. Lett.* **95**, 040602 (2005).
18. T. R. Gingrich, G. M. Rotskoff, J. M. Horowitz, Inferring dissipation from current fluctuations. *J. Phys. A* **50**, 184004 (2017).
19. J. M. Horowitz, T. R. Gingrich, Thermodynamic uncertainty relations constrain non-equilibrium fluctuations. *Nat. Phys.* **16**, 15–20 (2020).
20. P. Talkner, P. Hänggi, Colloquium: Statistical mechanics and thermodynamics at strong coupling: Quantum and classical. *Rev. Mod. Phys.* **92**, 041002 (2020).
21. P. Hänggi, F. Marchesoni, Artificial Brownian motors: Controlling transport on the nanoscale. *Rev. Mod. Phys.* **81**, 387–442 (2009).
22. W. Bialek, S. Setayeshgar, Physical limits to biochemical signaling. *Proc. Natl. Acad. Sci. U.S.A.* **102**, 10040–10045 (2005).
23. R. Marsland, W. Cui, J. M. Horowitz, The thermodynamic uncertainty relation in biochemical oscillations. *J. R. Soc. Interface* **16**, 20190098 (2019).
24. R. Rao, M. Esposito, Nonequilibrium thermodynamics of chemical reaction networks: Wisdom from stochastic thermodynamics. *Phys. Rev. X* **6**, 041064 (2016).
25. G. Lan, P. Sartori, S. Neumann, V. Sourjik, Y. Tu, The energy–speed–accuracy trade-off in sensory adaptation. *Nat. Phys.* **8**, 422–428 (2012).
26. J. Li, J. M. Horowitz, T. R. Gingrich, N. Fakhri, Quantifying dissipation using fluctuating currents. *Nat. Commun.* **10**, 1666 (2019).
27. U. Seifert, From stochastic thermodynamics to thermodynamic inference. *Annu. Rev. Condens. Matter Phys.* **10**, 171–192 (2019).
28. M. Esposito, Stochastic thermodynamics under coarse graining. *Phys. Rev. E* **85**, 041125 (2012).
29. I. A. Martínez, G. Bisker, J. M. Horowitz, J. M. R. Parrondo, Inferring broken detailed balance in the absence of observable currents. *Nat. Commun.* **10**, 3542 (2019).
30. E. Roldán, J. M. R. Parrondo, Estimating dissipation from single stationary trajectories. *Phys. Rev. Lett.* **105**, 150607 (2010).
31. F. Bai et al., Conformational spread as a mechanism for cooperativity in the bacterial flagellar switch. *Science* **327**, 685–689 (2010).
32. T. Mitchison, M. Kirschner, Dynamic instability of microtubule growth. *Nature* **312**, 237–242 (1984).
33. B. Lacroix et al., In situ imaging in *C. elegans* reveals developmental regulation of microtubule dynamics. *Dev. Cell* **29**, 203–216 (2014).
34. K. Thurley et al., Reliable encoding of stimulus intensities within random sequences of intracellular Ca^{2+} spikes. *Sci. Signal.* **7**, ra59 (2014).
35. U. Seifert, Stochastic thermodynamics, fluctuation theorems and molecular machines. *Rep. Prog. Phys.* **75**, 126001 (2012).
36. J. M. R. Parrondo, C. V. den Broeck, R. Kawai, Entropy production and the arrow of time. *New J. Phys.* **11**, 073008 (2009).

37. C. Maes, F. Redig, M. Verschuere, No current without heat. *J. Stat. Phys.* **106**, 569–587 (2002).
38. J. Gladrow, N. Fakhri, F. C. MacKintosh, C. F. Schmidt, C. P. Broedersz, Broken detailed balance of filament dynamics in active networks. *Phys. Rev. Lett.* **116**, 248301 (2016).
39. C. Battle *et al.*, Broken detailed balance at mesoscopic scales in active biological systems. *Science* **352**, 604–607 (2016).
40. G. Bisker, M. Polettni, T. R. Gingrich, J. M. Horowitz, Hierarchical bounds on entropy production inferred from partial information. *J. Stat. Mech.* **2017**, 093210 (2017).
41. I. Lestas, G. Vinnicombe, J. Paulsson, Fundamental limits on the suppression of molecular fluctuations. *Nature* **467**, 174–178 (2010).
42. A. C. Barato, U. Seifert, Thermodynamic uncertainty relation for biomolecular processes. *Phys. Rev. Lett.* **114**, 158101 (2015).
43. T. R. Gingrich, J. M. Horowitz, N. Perunov, J. L. England, Dissipation bounds all steady-state current fluctuations. *Phys. Rev. Lett.* **116**, 120601 (2016).
44. F. S. Gnesotto, G. Gradziuk, P. Ronceray, C. P. Broedersz, Learning the non-equilibrium dynamics of Brownian movies. *Nat. Commun.* **11**, 5378 (2020).
45. S. Otsubo, S. K. Manikandan, T. Sagawa, S. Krishnamurthy, Estimating entropy production along a single non-equilibrium trajectory. arXiv [Preprint] (2020). <https://arxiv.org/abs/2010.03852> (Accessed 22 April 2021).
46. D. K. Kim, Y. Bae, S. Lee, H. Jeong, Learning entropy production via neural networks. *Phys. Rev. Lett.* **125**, 140604 (2020).
47. T. Van Vu, V. T. Vo, Y. Hasegawa, Entropy production estimation with optimal current. *Phys. Rev. E* **101**, 042138 (2020).
48. M. Campisi, L. Buffoni, Dissipation and asymmetry in non-equilibrium processes. arXiv [Preprint] (2020). <https://arxiv.org/abs/2011.01076> (Accessed 22 April 2021).
49. M. Polettni, M. Esposito, Effective thermodynamics for a marginal observer. *Phys. Rev. Lett.* **119**, 240601 (2017).
50. É. Roldán, J. Barral, P. Martin, J. M. R. Parrondo, F. Jülicher, Arrow of time in active fluctuations. arXiv [Preprint] (2018). <https://arxiv.org/abs/1803.04743> (Accessed 22 April 2021).
51. S. K. Manikandan, D. Gupta, S. Krishnamurthy, Inferring entropy production from short experiments. *Phys. Rev. Lett.* **124**, 120603 (2020).
52. J. A. Nirody, A. L. Nord, R. M. Berry, Load-dependent adaptation near zero load in the bacterial flagellar motor. *J. R. Soc. Interface* **16**, 20190300 (2019).
53. J. Paulsson, Summing up the noise in gene networks. *Nature* **427**, 415–418 (2004).
54. M. Skoge, S. Naqvi, Y. Meir, N. S. Wingreen, Chemical sensing by nonequilibrium cooperative receptors. *Phys. Rev. Lett.* **110**, 248102 (2013).
55. A. Sancar, L. A. Lindsey-Boltz, K. Ünsal-Kaçmaz, S. Linn, Molecular mechanisms of mammalian DNA repair and the DNA damage checkpoints. *Annu. Rev. Biochem.* **73**, 39–85 (2004).
56. J. J. Hopfield, Kinetic proofreading: A new mechanism for reducing errors in biosynthetic processes requiring high specificity. *Proc. Natl. Acad. Sci. U.S.A.* **71**, 4135–4139 (1974).
57. C. Jarzynski, Equalities and inequalities: Irreversibility and the second law of thermodynamics at the nanoscale. *Annu. Rev. Condens. Matter Phys.* **2**, 329–351 (2011).
58. H. Qian, S. Kjelstrup, A. B. Kolomeisky, D. Bedeaux, Entropy production in mesoscopic stochastic thermodynamics: Nonequilibrium kinetic cycles driven by chemical potentials, temperatures, and mechanical forces. *J. Phys. Condens. Matter* **28**, 153004 (2016).
59. H. Ge, H. Qian, Physical origins of entropy production, free energy dissipation, and their mathematical representations. *Phys. Rev. E* **81**, 051133 (2010).
60. N. G. Van Kampen, *Stochastic Processes in Physics and Chemistry* (Elsevier, 1992), vol. 1.
61. T. Franosch *et al.*, Resonances arising from hydrodynamic memory in Brownian motion. *Nature* **478**, 85–88 (2011).
62. V. Blickle, T. Speck, L. Helden, U. Seifert, C. Bechinger, Thermodynamics of a colloidal particle in a time-dependent nonharmonic potential. *Phys. Rev. Lett.* **96**, 070603 (2006).
63. Q. Liu, J. Wang, Quantifying the flux as the driving force for nonequilibrium dynamics and thermodynamics in non-Michaelis–Menten enzyme kinetics. *Proc. Natl. Acad. Sci. U.S.A.* **117**, 923–930 (2020).
64. S. Ciliberto, Experiments in stochastic thermodynamics: Short history and perspectives. *Phys. Rev. X* **7**, 021051 (2017).
65. P. Sartori, L. Granger, C. F. Lee, J. M. Horowitz, Thermodynamic costs of information processing in sensory adaptation. *PLoS Comput. Biol.* **10**, e1003974 (2014).
66. V. Y. Chernyak, M. Chertkov, C. Jarzynski, Path-integral analysis of fluctuation theorems for general Langevin processes. *J. Stat. Mech.* **2006**, P08001 (2006).
67. A. M. Jurgens, J. P. Crutchfield, Shannon entropy rate of hidden Markov processes. arXiv [Preprint] (2020). <https://arxiv.org/abs/2008.12886> (Accessed 22 April 2021).
68. A. M. Jurgens, J. P. Crutchfield, Functional thermodynamics of Maxwellian ratchets: Constructing and deconstructing patterns, randomizing and derandomizing behaviors. *Phys. Rev. Res.* **2**, 033334 (2020).
69. C. Maes, K. Netočný, B. Wynants, Dynamical fluctuations for semi-Markov processes. *J. Phys. A* **42**, 365002 (2009).
70. J. Zhang, T. Zhou, Markovian approaches to modeling intracellular reaction processes with molecular memory. *Proc. Natl. Acad. Sci. U.S.A.* **116**, 23542–23550 (2019).
71. D. Liberzon, *Calculus of Variations and Optimal Control Theory: A Concise Introduction* (Princeton University Press, 2011).
72. Z. Ugray *et al.*, Scatter search and local NLP solvers: A multistart framework for global optimization. *Inf. J. Comput.* **19**, 328–340 (2007).
73. F. Wang, J. Yuan, H. C. Berg, Switching dynamics of the bacterial flagellar motor near zero load. *Proc. Natl. Acad. Sci. U.S.A.* **111**, 15752–15755 (2014).
74. W. Hwang, M. Karplus, Structural basis for power stroke vs. Brownian ratchet mechanisms of motor proteins. *Proc. Natl. Acad. Sci. U.S.A.* **116**, 19777–19785 (2019).
75. S. Whitelam, K. Klymko, D. Mandal, Phase separation and large deviations of lattice active matter. *J. Chem. Phys.* **148**, 154902 (2018).
76. Y. Sowa, R. M. Berry, Bacterial flagellar motor. *Q. Rev. Biophys.* **41**, 103–132 (2008).
77. H. C. Berg, The rotary motor of bacterial flagella. *Annu. Rev. Biochem.* **72**, 19–54 (2003).
78. T. Ekeh, M. E. Cates, E. Fodor, Thermodynamic cycles with active matter. *Phys. Rev. E* **102**, 010101 (2020).
79. A. L. Nord *et al.*, Catch bond drives stator mechanosensitivity in the bacterial flagellar motor. *Proc. Natl. Acad. Sci. U.S.A.* **114**, 12952–12957 (2017).
80. E. Krasnopeeva, C. J. Lo, T. Pilizota, Single-cell bacterial electrophysiology reveals mechanisms of stress-induced damage. *Biophys. J.* **116**, 2390–2399 (2019).
81. J. G. Wakefield, C. A. Moores, A. J. Zwetsloot, G. Tut, A. Straube, Measuring microtubule dynamics. *Essays Biochem.* **62**, 725–735 (2018).
82. B. Lacroix *et al.*, Microtubule dynamics scale with cell size to set spindle length and assembly timing. *Dev. Cell* **45**, 496–511.e6 (2018).
83. H. Flyvbjerg, T. E. Holy, S. Leibler, Stochastic dynamics of microtubules: A model for caps and catastrophes. *Phys. Rev. Lett.* **73**, 2372–2375 (1994).
84. H. Bowne-Anderson, M. Zanic, M. Kauer, J. Howard, Microtubule dynamic instability: A new model with coupled GTP hydrolysis and multistep catastrophe. *Bioessays* **35**, 452–461 (2013).
85. J. Sneyd *et al.*, On the dynamical structure of calcium oscillations. *Proc. Natl. Acad. Sci. U.S.A.* **114**, 1456–1461 (2017).
86. J. F. Perez, M. J. Sanderson, The frequency of calcium oscillations induced by 5-HT, ACH, and KCl determine the contraction of smooth muscle cells of intrapulmonary bronchioles. *J. Gen. Physiol.* **125**, 535–553 (2005).
87. R. E. Dolmetsch, K. Xu, R. S. Lewis, Calcium oscillations increase the efficiency and specificity of gene expression. *Nature* **392**, 933–936 (1998).
88. X. Gu, N. C. Spitzer, Distinct aspects of neuronal differentiation encoded by frequency of spontaneous Ca²⁺ transients. *Nature* **375**, 784–787 (1995).
89. Y. J. Yang, H. Qian, Unified formalism for entropy production and fluctuation relations. *Phys. Rev. E* **101**, 022129 (2020).
90. H. Ge, H. Qian, Dissipation, generalized free energy, and a self-consistent nonequilibrium thermodynamics of chemically driven open subsystems. *Phys. Rev. E* **87**, 062125 (2013).
91. P. Sartori, Y. Tu, Free energy cost of reducing noise while maintaining a high sensitivity. *Phys. Rev. Lett.* **115**, 118102 (2015).
92. Y. Cao, H. Wang, Q. Ouyang, Y. Tu, The free-energy cost of accurate biochemical oscillations. *Nat. Phys.* **11**, 772–778 (2015).
93. H. Qian, Reducing intrinsic biochemical noise in cells and its thermodynamic limit. *J. Mol. Biol.* **362**, 387–392 (2006).
94. J. Yan, A. Hilfinger, G. Vinnicombe, J. Paulsson, Kinetic uncertainty relations for the control of stochastic reaction networks. *Phys. Rev. Lett.* **123**, 108101 (2019).